

Performance of Ceramics in Severe Environments

*Nathan S. Jacobson, Dennis S. Fox, James L. Smialek, and Christopher Dellacorte
NASA Glenn Research Center
Cleveland, OH 44135*

*Kang N. Lee
Cleveland State University/NASA Glenn Research Center
Cleveland, OH 44135*

Introduction

Ceramics are generally stable to higher temperatures than most metals and alloys. Thus the development of high temperature structural ceramics has been an area of active research for many years. While the dream of a ceramic heat engine still faces many challenges, niche markets are developing for these materials at high temperatures. In these applications, ceramics are exposed not only to high temperatures but also aggressive gases and deposits. In this chapter we review the response of ceramic materials to these environments. We discuss corrosion mechanisms, the relative importance of a particular corrodent, and, where available, corrosion rates.

Most of the available corrosion information is on silicon carbide (SiC) and silicon nitride (Si₃N₄) monolithic ceramics. These materials form a stable film of silica (SiO₂) in an oxidizing environment. We begin with a discussion of oxidation of these materials and proceed to the effects of other corrodents such as water vapor and salt deposits. We also discuss oxidation and corrosion of other ceramics—precursor derived ceramics, ceramic matrix composites (CMCs), ceramics which form oxide scales other than silica, and oxide ceramics. Many of the corrosion issues discussed can be mitigated with refractory oxide coatings and we discuss the current status of this active area of research. Ultimately, the concern of corrosion is loss of load bearing capability. We discuss the effects of corrosive environments on the strength of ceramics, both monolithic and composite. We conclude with a discussion of high temperature wear of ceramics, another important form of degradation at high temperatures.

The durability of ceramics is studied with a variety of techniques. Isothermal oxidation studies in air can be carried out in a simple box furnace. Formation of a protective surface oxide results in a weight gain, with oxidation kinetics determined by weight gain as a function of time.

Alternatively these kinetics can be derived from oxide thicknesses measured as a function of time

via optical (Ref. 1) and electron-optical techniques. Tube furnaces allow the use of controlled exposure environments. Thermogravimetric analysis (TGA) permits weight change to be continuously monitored (Ref. 2). Thermal cycling can be introduced to more accurately model a real application. High velocity, hydrocarbon-fueled burner rigs subject potential engine materials to an environment which closely approximates actual operating conditions. After these exposures samples are typically analyzed with a variety of techniques including optical microscopy, x-ray diffraction (XRD), and scanning electron microscopy (SEM) to determine composition and morphology of the corrosion products.

High Temperature Oxidation and Corrosion of Silica-Forming Ceramics

Isothermal Oxidation

In this section we discuss the kinetics of SiO₂ formation on Si, SiC, and Si₃N₄ in oxygen:



Figure 1 illustrates the formation of a protective oxide scale. The amount of oxide formed can be described in three different ways: the net weight change of the sample, the thickness of the oxide formed, and the recession into the starting material. Conversion of these quantities is given in Table I, assuming the loss of C or N from SiC and Si₃N₄, respectively. Figure 2 illustrates typical TGA results for high purity SiC and Si₃N₄ at 1300°C in pure oxygen. The raw data for this plot were taken as weight gain and the plot is in the form of scale thickness to provide a comparison between the two materials.

Material	Scale Thickness (μm)	Weight Gain (mg/cm^2)	Recession (μm)
Si-SiO ₂ (am)	1	0.1173	0.4406
Si-SiO ₂ (cr)	1	0.1237	0.4647
SiC-SiO ₂ (am)	1	0.0773	0.4808
SiC-SiO ₂ (cr)	1	0.0733	0.4583
Si ₃ N ₄ -SiO ₂ (am)	1	0.0516	0.6235
Si ₃ N ₄ -SiO ₂ (cr)	1	0.0489	0.5969

Table I. Conversion of scale thickness to weight gain and to recession for Si, SiC, and Si₃N₄.

(am) = amorphous; (cr) = cristobalite

A good deal can be learned from the oxidation of pure silicon to form surface SiO₂. This process has been extensively studied by the semiconductor industry (Ref. 3) and is relatively well-understood. The oxidation of silicon will be briefly summarized to provide a basis for the discussion of SiC and Si₃N₄ oxidation.

Silicon oxidation is described by reaction (1). Kinetic data can be accurately described with the linear-parabolic model of Deal and Grove (Ref. 3):

$$x_o^2 + Ax_o = B(t + \tau) \quad (4)$$

Here x_o is the thickness of the oxide, t is the time, τ is a shift in time to correct for the initial oxide layer, and A and B are constants related to the linear and parabolic rate constants. At short times, equation (2) reduces to:

$$x_o \cong \frac{B}{A}(t + \tau) \quad (5)$$

Thus the quantity B/A is the linear rate constant. It is generally agreed that in the early stages of oxidation, the rate controlling step is the chemical reaction (1). The linear rate constant can be fit to a standard Arrhenius expression:

$$\frac{B}{A} = \left(\frac{B}{A}\right)_o \exp\left(\frac{Q_L}{RT}\right) \quad (6)$$

Here $\left(\frac{B}{A}\right)_o$ is the pre-exponential, Q_L is the activation energy for the linear rate constant, R is the gas constant, and T is the absolute temperature. Table II lists a fit for some measured silicon linear rate constants. At longer times, equation (2) simplifies to:

$$x_o^2 \cong Bt \quad (7)$$

Here the quantity B is the parabolic rate constant. In this case the rate controlling step is diffusion through the oxide scale. Similarly the parabolic rate constant can be expressed with an Arrhenius rate expression:

$$B = B_o \exp\left(\frac{Q_p}{RT}\right) \quad (8)$$

Here B_o is the pre-exponential and Q_p is the activation energy for the parabolic rate constant. These are given in Table II.

Silica exists in crystalline as well as amorphous forms. Consider first the amorphous form which grows on silicon in pure oxygen at temperatures less than 1200°C. The network of silicon and oxygen atoms is sufficiently open so that there are channels for diatomic oxygen to permeate. Based on this concept, Deal and Grove (Ref. 3) derive the following expression for the parabolic rate constant:

$$B = \frac{2D_{eff}C^*}{N_l} \quad (9)$$

Here D_{eff} is the effective diffusion coefficient for permeation, C^* is the equilibrium concentration of oxidant in the oxide, and N_l is the number of oxidant molecules incorporated into a unit volume of the oxide layer. Using the permeation rates of diatomic oxygen through amorphous silica measured by Norton (Ref. 4), Deal and Grove are able to derive the oxidation rates of Si. These calculated rates show good agreement with measured parabolic rates.

Figure 3 is a standard Arrhenius plot of silicon oxidation compared to the oxidation rates for alloys which form other common protective oxides—alumina, Al_2O_3 (Ref. 5) and chromia, Cr_2O_3 (Ref. 6). This illustrates the unique properties of the silica scale. Note that the rates of silica formation are very low. More importantly, the activation energy for silica growth is low as permeation of oxygen through the silica network does not involve bond breaking, as a lattice diffusion process would. Thus the data indicate that SiO_2 is one of the best protective oxides in a pure oxygen environment.

Oxidation of SiC also follows linear-parabolic kinetics. The linear rate constant has only been measured by a few investigators and is listed in Arrhenius form in Table II. Linear regimes are only observable at temperatures less than about 1200°C. Oxidation occurs via the following reactions:



Motzfeld (Ref. 7) was the first to point out that the oxidation rates of SiC should be 1.5 to 2 times slower than the oxidation rates of silicon due to the additional oxygen needed to oxidize the carbon, as shown in reactions (7a) or (7b) respectively. This has been verified experimentally (Refs. 1,7). Further, as indicated in Table I the activation energy for the parabolic rate constants of Si and SiC are similar, suggesting a permeation mechanism for diffusion control through the SiO₂ scale.

Parabolic rate constants for SiC are also listed in Table II (Refs. 1,8). One important observation with SiC is the oxidation rate dependence on crystallographic orientation (Ref. 1). The reasons for this are controversial. Harris (Ref. 9) suggested this occurs only during the linear oxidation period and is due to different chemical reaction rates. Costello and Tressler (Ref. 10) and Zheng et al. (Ref. 11) observe this during the parabolic regime. Ramberg et al. (Ref. 1) see evidence of a silicon oxycarbide subscale, which may influence the diffusion rate, though its existence has not been clearly established.

At short times and temperatures below ~1200°C, the thermally grown SiO₂ film is amorphous. A number of factors lead to crystallization of SiO₂, including longer times, higher temperatures, and impurities. A key question becomes the effect of crystallinity on oxidation rates. Ogbuji (Ref. 12) has performed experiments on oxidation of SiC at 1300°C with an *in-situ*, long-term anneal to transform the scale from amorphous to crystalline. Oxidation rates decrease by a factor of ~30X upon crystallization. Further, even though crystalline scale occupies a portion of the total scale, new amorphous scale is continually growing. Thus crystallization decreases oxidation rates, but only by a small amount. This contrasts with Al₂O₃ scales where crystallization from the θ phase to the α phase leads to a two order of magnitude decrease in oxidation rates (Ref. 13).

The discussion thus far has been on coupons and plates of Si and SiC. Generally, the oxidation rates of powders scale accordingly with surface area (Ref. 14). However, nano-particles of Si (20

to 500 nm) have been shown to oxidize more slowly than expected (Ref. 15). The observed rates do not fit the classical models (Ref. 3) and the reasons for the slower oxidation rates remain an interesting question.

Table II also lists oxidation rates for CVD and additive-containing Si_3N_4 (Refs. 8,16). It is instructive to first examine high purity Si_3N_4 and compare its rate to that of Si and SiC. The oxidation rate of Si_3N_4 is slower than that of SiC (Figure 1) and has a different activation energy than that of Si and SiC. This suggests that a different oxidation process occurs, although the exact mechanism has been an area of some controversy. High purity Si_3N_4 forms an intermediate silicon oxynitride layer of composition $\text{Si}_2\text{N}_2\text{O}$. The role of this intermediate is still unclear. Some investigators (Ref. 17) believe it acts as a diffusion barrier, leading to the slower reaction rates; other investigators (Ref. 18) believe it contributes to mixed diffusion/chemical reaction control of the oxidation process. Ogbuji and Jayne (Ref. 19) show evidence that the silicon oxynitride, written as $\text{SiN}_{2-x}\text{O}_{2+x}$, is actually a graded composition from Si_3N_4 to SiO_2 . They propose that oxidation occurs in this material as a progressive oxygen-for-nitrogen substitution.

Compound	Linear (B/A) ($\mu\text{m/hr}$) (Temperature K)	Ref.	Parabolic (B) ($\mu\text{m}^2/\text{hr}$) (Temperature K)	Ref.
Si	$8.713 \times 10^6 \exp(-195800/RT)$ 973-1473	3	$1296.05 \exp(-124000/RT)$ 1073-1473	3
Single Crystal SiC—Fast	$1.09 \times 10^5 \exp(-159000/RT)$ 1073-1373	1	$864 \exp(-99300/RT)$ 1073-1373	1
Single Crystal SiC—Slow			$8.94 \times 10^7 \exp(-292000/RT)$ 1073-1373	1
CVD Polycrystalline SiC			$285 \exp(-117800/RT)$ 1473-1773	8
CVD Polycrystalline Si_3N_4			$5.363 \times 10^9 \exp(-363900/RT)$ 1473-1773	8
SN282 Si_3N_4			$2.16 \times 10^5 \exp(-204600/RT)$ 1473-1673	15
AS 800 Si_3N_4			$3560 \exp(-131900/RT)$ 1473-1673	15

Table II. Linear and parabolic oxidation rate constants for Si, SiC, and Si_3N_4 in dry oxygen. Note that $R = 8.314 \text{ J/mol}\cdot\text{K}$

Most commercial forms of Si_3N_4 contain additives, typically refractory oxides, to promote densification. It has been shown that the effects of these impurities dominate oxidation (Refs. 20-22). In these cases movement of the additive cation (e.g. Mg^{+2} or Y^{+3}) outward into the growing oxide film is the rate-controlling step for oxidation. Typically these materials oxidize faster than high purity Si_3N_4 as shown in Table II. Many commercial forms of SiC also contain additives. In general boron and carbon additives in SiC lead to materials with oxidation rates comparable to those of high purity SiC (Ref. 10); however refractory oxide additives lead to materials with more rapid oxidation rates (Ref. 23).

Cyclic Oxidation

The discussion thus far has dealt with isothermal oxidation. However, many applications involve temperature cycling. This leads to stress from the thermal expansion mismatch between the substrate and the growing oxide scale. Figure 4 is a plot of the thermal expansion of crystalline SiO_2 (cristobalite), SiC, Si_3N_4 , and amorphous SiO_2 (Ref. 24). As noted, for most practical applications the scale will contain at least some amount of crystalline SiO_2 . Assuming a stress-free scale at temperature, the larger thermal expansion of the crystalline SiO_2 means that on cooling the scale on a SiC or Si_3N_4 substrate will be in tension. This leads to cracks on cooling, but these cracks heal in the next temperature increase. This behavior is in contrast to superalloys where the oxide is in compression on cooling, leading to oxide buckling and spallation. Thus cyclic oxidation behavior of SiC and Si_3N_4 tends to be good, as illustrated in Figure 5 (Refs. 25,26).

Corrosion of Silica-Forming Ceramics by Water Vapor

Many high temperature environments contain water vapor. In general, combustion of hydrocarbon fuels in air leads to an environment with ~10% water vapor (Ref. 24). At one bar total pressure this is ~0.1 bar water vapor and it scales accordingly to higher total pressures. Clearly the effects of water vapor on silica-forming ceramics must be understood to utilize these materials in such environments.

The fundamental studies of pure Si are again helpful to understand the effect of water vapor on SiC and Si_3N_4 oxidation. Deal and Grove (Ref. 3) have shown that silicon oxidizes more rapidly

in water vapor. The diffusivity of water vapor in silica is less than the diffusivity of oxygen in silica; however the solubility of water vapor in silica is considerably higher than that of oxygen. According to equation (9), this leads to a net increase in oxidation rate. A similar effect is observed for SiC oxidation (Ref. 27).

A second important effect of water vapor is that it can transport impurities from the environment to the sample (Ref. 27). As will be discussed, the oxidation of silica-forming ceramics is quite susceptible to secondary elements. Thus the study of water vapor effects requires a clean furnace, e.g. a silica furnace tube and pre-heating of any alumina parts to remove sodium impurities.

Perhaps the most important effect of water vapor at high temperatures is the formation of volatile species from the thermally grown SiO₂ scale (Refs. 28,29):



Thus as the scale grows, it is also volatilized by the water vapor in the stream. This leads to parabolic kinetics where the scale grows according to a parabolic rate law and the scale volatilizes according to a linear rate. The parabolic rate constant, k_p , has been discussed in an earlier section. In a flowing gas, volatilization is limited by the boundary layer. The rate of scale removal is linear with time according to the following expression for laminar flow over a flat plate (Ref. 30):

$$k_l = 0.664(Re)^{0.5} (Sc)^{0.33} \frac{D\rho_v}{L} \quad (13)$$

Here k_l is the linear rate constant, Re is the Reynolds number, Sc is the Schmidt number, D is the interdiffusion coefficient of the volatile specie (primarily Si(OH)₄(g)) in the boundary layer, ρ_v is the density of the volatile specie in the boundary layer, and L is a characteristic dimension of the specimen. Combined parabolic growth kinetics and linear volatilization kinetics leads to:

$$\frac{dx}{dt} = \frac{k_p}{x} - k_l \quad (14)$$

Here x is the scale thickness and t is time. Figure 6 illustrates this behavior via TGA measurements in a 50% O₂/50% H₂O environment (Ref. 25) at 1200°C. The SiO₂ specimen shows a linear weight loss. Both the SiC and Si₃N₄ initially show a weight gain, followed by a weight loss at a rate similar to that of the SiO₂ specimen. Note the initial weight gain of SiC is greater than that of Si₃N₄ due to the faster oxidation rate of SiC. It is important to note that over

long times, the SiC and Si₃N₄ substrate will exhibit greater recession as a result of this oxidation/volatilization process relative to oxidation alone.

The above description of scale volatility can be extended to a hydrocarbon fuel burner (Refs. 31-33). Figure 7 illustrates some kinetic results for SiC under these conditions. These weight losses are primarily due to the volatility of the SiO₂ film according to reaction (12). From equation (13) the key dependences on velocity, v ; temperature, T ; and pressure, P can be extracted:

$$k_l \propto \frac{v^{0.5}}{P_{total}^{0.5}} P(Si(OH)_4) \propto v^{0.5} P_{total}^{1.5} \quad (15)$$

Here v is the gas velocity, P_{total} is the total pressure, and $P(Si(OH)_4)$ is partial pressure of Si(OH)₄(g). According to equation (12), the partial pressure of Si(OH)₄ is proportional to the square of water vapor pressure, which is proportional to total pressure for hydrocarbon fuel burners. This fact leads to the simplified expression on the right hand side of equation (15). The linear rate constant would be expected to have an exponential dependency on temperature as the vapor pressure, $P(Si(OH)_4)$, varies exponentially with temperature.

The normalized Arrhenius representation of k_l in Fig. 8 was obtained from multiple linear regression over a range of pressure, gas velocity, and temperature test conditions, yielding an empirical weight loss equation in a form similar to equation (15):

$$k_l (mg / cm^2 - hr) = 2.06 \exp\left(\frac{108000 J / mol}{RT}\right) P_{total}^{1.5} v^{0.5} \quad (16)$$

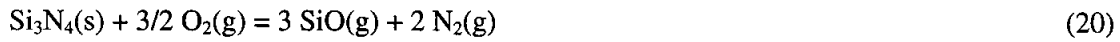
Here T is temperature in degrees K, P is pressure in atmospheres, and v is velocity in meter/sec. Equivalent relationships were measured (and derived) for recession of SiC in $\mu\text{m}/\text{hr}$, represented by multiplying equation (16) by 2.9 (3.1, for the derived equation). Rates for three types of SiC composites were found to be equivalent to CVD SiC or sintered SiC (Ref. 34). The volatility rates determined for CVD and sintered Si₃N₄ were both found to be 1.8 times those of SiC, with no apparent effect of additives or the oxynitride interface layer (Ref. 35).

Equation (16) must be modified to include slightly different water vapor contents in actual turbine engines (changes in fuel-to-air ratio and/or water injection). By normalizing to the calculated equilibrium water content in the burner rig (0.10-0.12 atm.), equation (16) can be re-written in general form as:

$$k_1(\text{mg} / \text{cm}^2 - \text{hr}) = 177 \exp\left(\frac{108000 \text{ J} / \text{mol}}{RT}\right) \frac{[P(\text{H}_2\text{O})]^2 v^{0.5}}{P_{\text{Total}}^{0.5}} \quad (17)$$

Active Oxidation

In addition to condensed phase SiO_2 , silicon-based ceramics also form a stable volatile sub-oxide, $\text{SiO}(\text{g})$. In a flowing gas stream at low oxygen partial pressures, formation of $\text{SiO}(\text{g})$ —known as active oxidation—can be a rapid mode of degradation (Refs. 36,37):



It is essential to delineate the conditions when SiO_2 formation (passive oxidation) no longer occurs and a transition to $\text{SiO}(\text{g})$ occurs. There are many studies of these transitions in the literature.

It is again useful to begin with an understanding of the active/passive transition for silicon, as discussed by Wagner (Ref. 36). An important point is the difference between the active-to-passive and passive-to-active transitions, with the former generally several orders of magnitude greater than the later. As oxidant pressure is gradually raised, silicon first oxidizes to $\text{SiO}(\text{g})$ and eventually undergoes an active-to-passive transition when $\text{SiO}_2(\text{s})$ forms. Wagner derives this based on the condition that there be sufficient oxygen to form the $\text{SiO}(\text{g})$ required by the equilibrium between Si and SiO_2 :



Wagner assumes that the flux of oxygen approaching the bare silicon surface is boundary-layer limited and develops expressions for $P_{\text{active-to-passive}}^{\text{transition}}(\text{O}_2)$ based on this. On the other hand, the passive-to-active transition occurs as pressure is gradually decreased to the point where $\text{SiO}_2(\text{s})$ decomposes:



Thus a transition oxygen pressure can be calculated from the above equation.

This general approach has been extended to SiC and Si_3N_4 by a number of investigators (Refs. 26, 37-45). Conditions for scale/substrate equilibrium analogous to equation (21) can be written as:





Figure 9 illustrates the transitions for SiC with the two boundaries indicated (defined by reactions (23) and (21) above) listed and experimental data presented from selected studies. There is a good deal of research in this interesting phenomenon and many theories exist on the details of the transitions. However the important issue is that at low oxidant pressures, SiC and Si₃N₄ are not stable and can rapidly degrade due to volatile SiO(g) formation.

Related to active oxidation is the actual reaction of the SiO₂ scale and SiC or Si₃N₄ substrate at very high temperatures, according to reactions (23) and (24) (Ref. 46). This is near the melting point of the SiO₂ scale (1996 K), which is well-above the useful application temperature of these ceramics. These reactions lead to extensive gas generation and scale bubbling and could lift the oxide scale.

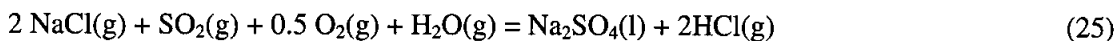
Effects of Low Level Impurities

In various applications low levels of metallic impurities are very common. These can induce crystallization of amorphous silica. In addition, alkali cations necessarily provide additional oxygen anions and act as network modifiers, creating non-bridging oxygen anions which open up the structure of the silica network. This translates to higher oxygen permeation rates. Small amounts of sodium cations will increase oxidation rates by an order of magnitude (Refs. 47-50).

Recent studies (Refs. 51-53) indicate that optimized levels of implanted aluminum can counter this effect of sodium by bridging the oxygen anions. This leads to lower oxidation rates and more uniform SiO₂ scale morphologies. In addition, aluminum implanted ions can decrease the oxidation rates of additive-containing Si₃N₄ (Ref. 53). As discussed in section II, outward diffusion of the additive cations such as Mg⁺² is rate controlling. It appears that Al retards this outward diffusion at temperatures of 1000°C or less. However at higher temperatures, the effect is limited due to the appearance of liquid-like phases.

Molten Salt Corrosion

In many practical situations such as heat engines and heat exchangers, condensed phase deposits will form. The most important type of deposit is sodium sulfate (Na_2SO_4) which forms from the combination of sodium impurities in the air or fuel with sulfur impurities in the fuel (Ref. 54):



This type of deposit-induced corrosion is termed “hot corrosion” and there is a large amount of literature on the hot corrosion of metals (Refs. 54,55). In addition to Na_2SO_4 -induced hot corrosion, other deposits, such as calcium sulfate, sodium vanadate, and oxide slags can induce corrosion (Ref. 26). The focus here will be on Na_2SO_4 -induced corrosion; however, the basic principles discussed carry through to other systems.

Hot corrosion attack occurs in two steps (1) deposition and (2) corrosive attack. Generally Na_2SO_4 is most corrosive above its melting point (1157 K) but below its dewpoint. The dewpoint is related to sulfur and sodium contents together with the total pressure. Dewpoints can be calculated using a free-energy minimization code (Refs. 57) and are shown in Figure 10 (Ref. 58). In general the range of Na_2SO_4 attack is narrow (typically only 100 K, with higher pressures increasing the dew point and temperature range), but it can be quite severe when it does occur.

A laboratory simulation of deposition and corrosive attack is challenging and various methods have been used. Important issues include continuous deposition as well as temperature, pressure and velocity effects. The closest simulation to a heat engine is a fuel burner seeded with salt to form Na_2SO_4 (Ref. 59). However such tests are expensive and it is difficult to control all parameters. The most common laboratory test is airbrushing an aqueous Na_2SO_4 solution on the sample and allowing the water to evaporate and leave a thin film of Na_2SO_4 . The sample is exposed in a furnace, ideally with a set pressure of SO_3 (or SO_2/O_2) to establish a fixed activity of Na_2O (Ref. 60). Such a test is easily conducted and allows accurate control of parameters, but a one-time deposition of Na_2SO_4 may not be an adequate simulation of an actual heat engine situation. Other laboratory tests involve a two zone furnace where a container of salt is heated in one zone and the sample is placed in another zone (Ref. 61). Such tests are more complex, but create a more realistic continuous deposition situation.

Hot corrosion is generally described both by a sulfidation and/or an oxide fluxing mechanism (Ref. 56). Condensed phase silicon sulfide is not a thermodynamically stable compound so the sulfidation mechanism is not applicable to silicon-based ceramics. However the process is

described very well by an oxide fluxing mechanism. The reactive component of Na_2SO_4 is Na_2O formed by:



Consider the acid/base properties of oxides (Ref. 62). A low thermodynamic activity of Na_2O [$a(\text{Na}_2\text{O})$], set by a high partial pressure of SO_3 [$P(\text{SO}_3)$], is termed an acidic molten salt. A high thermodynamic activity of Na_2O , set by a low $P(\text{SO}_3)$, is termed a basic molten salt. Given a $P(\text{SO}_3)$, the thermodynamic activity of Na_2O follows from the free energy for reaction (26) (Ref. 63).

$$\Delta G = 526500 - 118T = -RT \ln K_p = -RT \ln a(\text{Na}_2\text{O})P(\text{SO}_3) \quad (27)$$

SiO_2 is a strongly acidic oxide (Ref. 62) and it reacts readily with basic Na_2O :



Figure 11 is a calculated phase diagram for the Na_2O - SiO_2 system and indicates the various sodium silicates formed at a particular temperature and activity of Na_2O , using the free energy minimization code and databases described in Ref. 63. Consider the bold line between the most silica-rich sodium silicates and silica. This boundary provides a convenient method to predict dissolution of silica. If the $P(\text{SO}_3)$ over the Na_2SO_4 deposit leads to $a(\text{Na}_2\text{O})$ greater than that given by the boundary in the figure, then dissolution will occur. This method has been used in a model situation in a burner to predict the behavior of quartz and fuels with different sulfur levels. The higher sulfur fuel (i.e. diesel) led to a low $a(\text{Na}_2\text{O})$ and hence limited attack; whereas the lower sulfur fuel (i.e. Jet A) led to a higher $a(\text{Na}_2\text{O})$ and hence dissolution (Ref. 58). While the use of higher sulfur fuels is not a practical way to control corrosion, it does confirm and illustrate the mechanism described by equations (26) and (28).

The concept of acid/base reactions with oxides is central to understanding hot corrosion of ceramics. It has been shown that free carbon will drive sodium sulfate more basic, by creating a larger concentration and therefore activity of Na_2O (Ref. 58). This is important as many ceramics contain carbon. In general SiC tends to corrode more readily than Si_3N_4 in Na_2SO_4 , primarily because the carbon drives the Na_2SO_4 more basic.

Reaction (28) above indicates the conversion of a solid, protective SiO_2 film to a liquid sodium silicate. Transport rates of oxygen through the liquid sodium silicate are much faster than transport of oxygen through solid SiO_2 , so the underlying SiC or Si_3N_4 oxidizes readily creating more SiO_2 for dissolution. Hot corrosion is best described coupling of reactions (2) or (3) with

reaction (28). With a one-time deposition of a basic Na_2O -containing deposit, it has been shown that these reactions continue until the liquidus boundary of $\text{Na}_2\text{O}\cdot x(\text{SiO}_2)(\text{l})/\text{SiO}_2(\text{s})$ is reached (Ref. 64). After the corrosion products are enriched in SiO_2 to reach this boundary, the reaction slows. The resultant structure is shown in Figure 12. However, in a continuous deposition situation, there is no limit on the coupled oxidation/dissolution reactions. This leads to very thick scales and substantial consumption of the ceramic. Figure 13 is a macro-view of two coupons of SiC—one oxidized in a burner with no added salt and one oxidized with 2 ppm Na. Note the very thick sodium silicate layer on the second coupon.

As Figure (13) suggests, the kinetics of this process are rapid due to presence of a liquid film. The thick film formed in Figure 13 suggest rates of consumption several orders of magnitude greater than pure oxidation. Sun et al. (Ref. 61) have performed controlled experiments on the corrosion of Si_3N_4 , using NaNO_3 as a source of Na_2O . They found linear reaction rates, indicating that diffusion is so rapid that the interface oxidation reaction controls the rate.

Other deposits result in similar behavior. The major issue is that basic salt or slag deposits dissolve SiO_2 and lead to consumption of SiC and Si_3N_4 . This has been observed with basic oxide slags from coal (Ref. 65). In these low oxygen situations, localized metal silicides also form from reaction of the silicon component with iron and nickel.

Oxidation of Precursor-Derived Silica-Forming Ceramics

Silicon carbonitrides are a new class of amorphous ceramic materials derived from polymer precursors. With the addition of boron, glass transition temperatures are as high as 1800°C (Ref. 66). Initial oxidation kinetic studies of these materials by weight change methods alone suggested extremely low oxidation rates (Ref. 67). However it is important to recognize that weight gains alone do not indicate oxidation behavior as concurrent volatilization of B, C, and N constituents would reduce the measured weight gains (Refs. 68,69). Also, in their present state these materials are porous, so the effects of internal oxidation must be understood (Ref. 66). Finally, inhomogenities lead to non-uniform oxidation behavior. Nonetheless there are methodical studies (Ref. 68) of these materials which separate the various contributions to observed weight losses. These indicate that the oxidation rates are comparable to those of high

purity SiC and Si₃N₄. As processing of these materials improves, more systematic studies of this interesting class of materials should be possible.

Oxidation of Composites and Non-Silica-Forming Ceramics

Oxidation of Silica-Forming Composites

The monolithic ceramics discussed thus far are generally low toughness materials, i.e. show limited resistance to failure from a pre-existing crack. A variety of composite materials based on silica-forming ceramics have been developed with the goal of increasing toughness (Refs 70,71). These include various types of fiber or particulate reinforcements, though the largest increase in toughness is attained with continuous fiber reinforcements. The matrix may be SiC or, Si₃N₄; the fibers are typically high strength SiC or C. The fibers deflect matrix cracks, which will increase toughness. However the fibers must not bond with the matrix. Carbon fibers do not bond with a SiC matrix, while SiC fibers are typically coated with either graphitic carbon or boron nitride to prevent bonding. Thus the system contains both slowly oxidizing phases (SiC, Si₃N₄) and rapidly oxidizing phases (C or BN). Understanding the oxidation behavior of these complex systems is essential to their application.

Consider first the situation of carbon fiber reinforced SiC. Several investigators (Refs. 72,73) have shown that at low temperatures oxidation is controlled by the chemical reaction rate of oxygen with carbon. At intermediate temperatures diffusion through the crack becomes rate controlling. At the highest temperatures the matrix is sealed due to SiO₂ formation. Reaction control leads to more uniform attack of the carbon fibers throughout the material, whereas diffusion control leads to localized attack of the carbon fibers.

Figure 14 illustrates weight loss curves for a composite of carbon-coated SiC fibers in a Si₃N₄ matrix (Ref. 74). Note that at 1400° and 1200°C, oxidative attack of the carbon coating is rapid and the composite quickly seals. At 600, 800, 1000°C, oxidative attack is less rapid and at 600 and 800°C the composite does not appear to seal. Filipuzzi et al. have modeled oxidation of carbon-coated SiC fibers in a SiC matrix (Refs. 75,76). They develop an analytical model for diffusion of oxygen into the pore between the matrix and fiber, created as the carbon fiber coating

oxidizes. They include the growth of silica on the matrix and fiber, which eventually seals the pore. Their analysis indicates that thinner fiber coatings give better performance.

In theory, BN fiber coatings should be an improvement over C coatings as the oxidation products of BN are not all volatile:



However, the problem here is the liquid B_2O_3 product. The $\text{B}_2\text{O}_3(\text{l})$ can further react with SiO_2 to form low melting silicates or it can react with water vapor to form highly stable volatile boron hydroxides (Ref. 77). This is illustrated in Figure 15, which shows (a) liquid borosilicate products and (b) absence of BN coating due to oxidation/volatilization.

The high toughness of these CMCs make them one of the most promising high temperature materials. However, understanding and mitigating their oxidation properties remains a critical issue.

Oxidation and Corrosion of Non-Silica-Forming Nitrides, Carbides, and Borides

In dry oxygen, aluminum nitride (AlN) oxidizes at rates comparable to Ni-Al alloys (Ref. 78). However, even small amounts of water vapor lead to rapid oxidation due to the formation of 20-100 nm micropores in the alumina scale. This issue has limited the application of AlN ceramics.

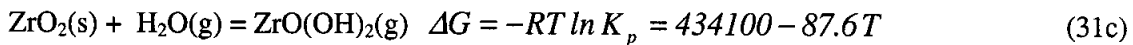
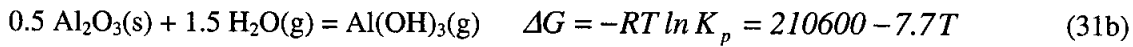
As noted, boron nitride (BN) is a potential fiber coating in ceramic matrix composites. It has been shown that the oxidation rates are quite dependent on such factors as porosity, oxygen content, and crystallinity of the starting material (Ref. 79). BN oxidizes to B_2O_3 , which is not a desirable protective oxide due to its low melting point and high reactivity with water vapor.

Transition metal carbides, nitrides, and borides have a number of important properties including high melting points, hardness, wear resistance, and high temperature strength. However, these form oxides with high oxygen diffusivities and short circuit oxygen paths such as cracks and pores. The range of recession rates is given in Figure 16 (Ref. 80). More details can be found in a recent review and references contained therein (Ref. 26).

Corrosion of Oxide Ceramics

In general, oxides are the most stable ceramics. Useful oxide ceramics include silica, alumina (Al_2O_3), mullite ($3\text{Al}_2\text{O}_3 \cdot 2\text{SiO}_2$), various stabilized zirconia (ZrO_2) compositions, and composites with either oxide or non-oxide reinforcements in an oxide matrix. Luthra and Park (Ref. 81) have shown that SiC reinforced Al_2O_3 oxidizes rapidly at temperature of 1375-1575°C to form a complex reaction product mixture.

The interaction of common oxides with water vapor has been reviewed (Ref. 82) with volatilization rates in the following order: $\text{SiO}_2 > \text{Al}_2\text{O}_3 > \text{ZrO}_2$. The following thermodynamic data (Refs. 29,83,84) can be used to estimate the vapor pressure of the primary volatile specie:



Here ΔG is the free energy change, R is the gas constant, T is the absolute temperature, and K_p is equilibrium constant.

The effect of deposits on oxide ceramics has been reviewed by Pettit et al. (Ref. 85). In general the effects are less than those from deposit-induced corrosion on metals or silica-forming ceramics. Deposits of Na_2SO_4 lead to grain boundary attack of Al_2O_3 . Stabilized zirconias are used as coatings for both metals and ceramics. An important issue here is the possible attack of the stabilizing oxide by vanadate deposits (Ref. 86).

Environmental Barrier Coatings

Environmental barrier coatings (EBCs) protect silica-forming ceramics and composites from attack by corrosive species in combustion environments (Ref. 87). The key requirements for a successful EBC (Ref. 88) include: i) environmental stability, especially in water vapor; ii) coefficient of thermal expansion (CTE) match to the substrate; iii) chemical compatibility with the substrate; iv) phase stability; v) low thermal conductivity. Table III lists the CTE of SiC, Si_3N_4 , and current EBC materials (Ref. 89). A low thermal conductivity is needed to minimize coating thickness. Table IV lists the thermal conductivity of current EBC materials in their hot-pressed

forms. No material has yet been identified that satisfies all the requirements. As a result current EBCs have multi-layers in which each layer has a specific role.

Table III. CTE of Si-based ceramics and current EBC materials

Material	SiC	Si ₃ N ₄	Si	Mullite*	BSAS**	Y ₂ SiO ₅	Sc ₂ SiO ₅	Er ₂ SiO ₅	Yb ₂ SiO ₅
CTE (10 ⁻⁶ /C)	4.5 ~ 5.5	3 ~ 4	3.5 ~ 4.5	5 ~ 6	4 ~ 5	5 ~ 6	5 ~ 6	5 ~ 7	3.5 ~ 4.5

* 3 Al₂O₃-2 SiO₂

** 1-xBaO-xSrO-Al₂O₃-2SiO₂, 0 ≤ x ≤ 1

Table IV. Thermal conductivity of hot-pressed current EBC materials at 200 °C - 1400°C determined by a high heat flux laser rig

Material	YSZ	Mullite	BSAS	Mullite +BSAS	Y ₂ SiO ₅	Sc ₂ SiO ₅	Yb ₂ SiO ₅	Er ₂ SiO ₅
Thermal conductivity (W/m-k)	2.2 ~ 2.9	2.2 ~ 2.8	2.5 ~ 3.0	2.0 ~ 2.3	1.6 ~ 1.9	2.3 ~ 3.5	1.3 ~ 1.4	1.4 ~ 1.5

Processing

Currently plasma spraying is the most successful and most widely used process to apply EBCs (Refs. 88-90). The process is relatively cost-effective and can readily deposit both metals and ceramics with a wide range of compositions. Plasma-sprayed coatings typically exhibit excellent strain tolerance due to the layered microstructure and high porosity. One limitation is the difficulty in applying coatings on complex structures and on small inner surfaces due to the line-of-sight nature of this process. Electron beam physical vapor deposition (EB-PVD) has been used with great success for processing thermal barrier coatings (TBC) for metallic components in various heat engines, signifying its potential for EBC processing. Other coating processes being explored include chemical vapor deposition (CVD) (Refs. 91,92), sol-gel, and slurry coating (Ref. 93). The non-line-of-sight nature of these processes allows the application of EBCs on complex-shaped components.

Performance

EBCs with a Mullite-Based Layer

Mullite and Mullite+BSAS. Mullite has a good CTE match and chemical compatibility with SiC and Si₃N₄ ceramics (Refs. 87-90) and therefore constitutes a key component in most current EBCs. Conventional plasma-sprayed mullite coatings contain a significant amount of metastable, amorphous phase due to the rapid cooling of molten mullite during solidification on a cold substrate (Ref. 90). A subsequent exposure of the mullite coating to a temperature above ~1000°C causes crystallization of the amorphous phase. Shrinkage accompanies the crystallization, leading to cracking and delamination of the mullite coating. A modified plasma-spray process enables the deposition of crystalline mullite coating which dramatically improves its crack resistance and adherence (Ref. 90). A plasma-sprayed mullite coatings on SiC showed improved resistance to Na₂SO₄-induced corrosion as compared to uncoated SiC (Ref. 94). A CVD mullite showed similar results (Ref. 95). Further improvement in the crack resistance of plasma-sprayed mullite coatings is achieved by adding a second phase BSAS (Refs. 88,96). The improved crack resistance of the mullite+BSAS composite coating is attributed to the reduced coating tensile stress from the low modulus BSAS phase (Ref. 97). Introduction of a silicon bond coat further enhances the durability of the mullite coating, by improving its adherence (Refs. 88,96). The relatively high silica activity of mullite (0.3 ~ 0.4) causes the selective volatilization of silica and the partial recession of mullite in high velocity combustion environments (Ref. 98).

Mullite/YSZ. A water vapor-resistant overlay coating is applied over the mullite coating, where the overlay coating provides water vapor stability while the mullite coating provides the adherence. YSZ is a logical candidate for a top coat because it has been successfully used as a TBC for metallic components in gas turbine engines, indicating its water vapor stability. Figure 17 compares the weight change of SiC, plasma-sprayed mullite-coated SiC, and plasma-sprayed mullite/YSZ-coated SiC in a high pressure burner rig (1230°C, 6 atm, gas velocity = 24 m/s) (Ref. 97). Note the absence of weight loss in the mullite/YSZ-coated SiC, indicating the water vapor stability of YSZ in a high velocity combustion environments. However there are critical disadvantages of YSZ, including a high CTE and sintering. The stress due to the CTE mismatch and sintering causes severe cracking which provides an easy path for water vapor penetration, resulting in rapid oxidation and premature coating delamination (Ref. 97).

Mullite/BSAS and Mullite+BSAS/BSAS. BSAS has a low silica activity, a low CTE, and a low modulus (~100 GPa), key attributes for a successful EBC. The low silica activity leads to stability in water vapor, while the low CTE and low modulus lead to a low EBC stress. These EBCs exhibit dramatically improved durability compared to the mullite/YSZ EBC. Figure 18 shows a cross-section of plasma-sprayed Si/mullite+20 w/o BSAS/BSAS on a SiC/SiC composite after 1000 h at 1316°C (1h cycles) in 90% H₂O-balance O₂ furnace testing (Ref. 87). The EBC maintained excellent adherence and crack resistance. Pockets of glass developed within the BSAS top coat. These EBCs were applied on SiC/SiC composite combustor liners for Solar Turbine (San Diego, CA) Centaur 50s gas turbine engines under the Department of Energy (DOE) Ceramic Stationary Gas Turbines (CSGT) Program (Refs. 99,100). One engine used by Texaco in Bakersfield, CA, successfully completed a 14,000-h field test (~1,250°C maximum combustor liner temperature).

However, BSAS still tends to volatilize at high velocities and high temperatures. The EBC on Solar Turbine engines suffered significant BSAS recession in some areas after the 14,000-h test (Ref. 100). Another key issue is the chemical reaction between BSAS and the silica thermally grown on the Si bond coat. The BSAS-silica reaction produces a low-melting (~1300°C) glass, causing EBC degradation and premature failure at temperatures above ~1300°C (Ref. 96). Therefore, it is desirable to avoid the BSAS second phase in the mullite layer for long-term exposures at high temperatures ($T > 1300^{\circ}\text{C} \sim 1350^{\circ}\text{C}$)

Mullite/RE₂SiO₅ and Mullite+BSAS/RE₂SiO₅. Some rare earth silicates are excellent EBC top coat materials due to their low CTE, phase stability, and low silica activity. Volatility data (Refs. 89,101) indicate that rare earth monosilicates (RE₂SiO₅; RE = rare earth element) are significantly less volatile than BSAS in water vapor, by at least an order-of-magnitude, while the volatility of rare earth disilicates (RE₂Si₂O₇, RE = rare earth element) is similar to that of BSAS. Figure 19 shows a cross-section of plasma-sprayed Si/mullite/Yb₂SiO₅ on a SiC/SiC composite (1000 h) at 1380°C (1h cycles) in 90% H₂O-balance O₂. The EBC maintained crack resistance and superb adherence to this substrate, as well as to Si₃N₄.

EBCs without a Mullite-Based Layer

BSAS. As indicated earlier, BSAS is reactive with the silica thermally grown on SiC or Si₃N₄, forming a low melting eutectic (mp ~ 1300°C). This chemical reaction causes the build-up of a thick reaction zone and pore formation at the BSAS/substrate interface which renders a single layer of this material unsuitable for an EBC.

RE₂SiO₅, RE₂Si₂O₇, and Ta₂O₅. Plasma-sprayed RE₂SiO₅ (Ref. 88) and Ta₂O₅-based EBC (Ref 103) show good adherence on Si-based ceramics under thermal cycling in air. However, these coatings do not maintain the adherence in water vapor environments. Consequently, the substrate suffers rapid oxidation, forming a thick and sometimes porous scale. CVD Ta₂O₅ is unstable in an environment containing Na₂SO₄, rapidly reacting to form NaTaO₃ which subsequently interacts destructively with the underlying Si₃N₄ substrate to form a molten phase (Ref. 104).

Water Vapor Resistance of Candidate EBC Materials

As noted, one of the key issues in development of suitable oxide EBCs is water vapor resistance. As discussed in an earlier section, the necessary thermodynamic data are only available for a few oxides. However screening-type studies have been done for a range of systems using high water-content furnaces or pressurized burner rig tests. These are summarized in Table V (Ref. 105-110). This table indicates the superior performance of hafnia and zirconia compounds, followed by rare earth hafnates or zirconates, and then rare earth monosilicates. Rare earth disilicates are near the midrange of the spectrum, as are barium aluminosilicate, alumina, aluminum titanate, and aluminum silicate. Finally silica, chromia, and boria are among the common oxides most rapidly attacked by water vapor and are provided as a lower reference point. It should also be noted that this Table is a summary of data from several sources using different techniques and represents our current state of understanding. Nonetheless it provides some general guidelines in the development of EBCs.

It is generally agreed that silicon-based ceramics and composites will require some type of EBC for engine/combustion environment applications. The development of such coatings is still an active area of research.


Oxide	Reference	
ZrO ₂ (metastable tetragonal— 8(Y ₂ O ₃) · (ZrO ₂))	98, 105-108	 <div data-bbox="1084 835 1279 1024" style="border: 1px solid black; padding: 5px; text-align: center;">Decreasing Water Vapor Resistance</div>
2(Lu ₂ O ₃) · 3(ZrO ₂)	109	
2(Y ₂ O ₃) · 3(ZrO ₂)	109	
3(Yb ₂ O ₃) · 5(Al ₂ O ₃)	106	
3(Y ₂ O ₃) · 5(Al ₂ O ₃) (YAG)	106, 107	
Lu ₂ O ₃ · SiO ₂	89, 108	
Yb ₂ O ₃ · SiO ₂	89, 108	
Y ₂ O ₃ · SiO ₂	89, 108	
Al ₂ O ₃ · TiO ₂	105	
2(Lu ₂ O ₃) · 3(HfO ₂)	105	
Lu ₂ O ₃ · 2(SiO ₂)	104, 105, 108, 109	
Y ₂ O ₃ · 2(SiO ₂)	106, 109, 110	
Yb ₂ O ₃ · 2(SiO ₂)	89, 104-106	
Ba(Sr)O · Al ₂ O ₃ · 2(SiO ₂) (BSAS)	96, 99	
SrO · Al ₂ O ₃ · 2(SiO ₂) (SAS)	99	
Al ₂ O ₃	33, 104-106, 108, 110, 111	
3(Al ₂ O ₃) · 2(SiO ₂) (mullite)	96, 99, 104-108	
TiO ₂	105	
CaO · 2(Yb ₂ O ₃) · 3(SiO ₂)	104, 105	
x(CeO ₂) · (ZrO ₂)	110	
SiO ₂	28, 29, 31, 33, 110	
Cr ₂ O ₃	82	

Table V. Approximate order of water vapor resistance for a range of current EBC candidate oxides.

Effects of Oxidation and Corrosion on Mechanical Properties

Current silicon nitrides have room temperature flexural strengths of 600-800 MPa (Refs. 112,113), with sintered α -SiC \sim 400 MPa (Ref. 114). Because these ceramics are inherently brittle, strength is a function of surface morphology. After 4500 h at 1200°C, sintered α -SiC exhibits a strength increase due to flaw healing, while alumina-containing SiC experiences a 50% strength loss due to pitting and oxide penetration along the grain boundaries (Ref. 115). Oxidized Si_3N_4 has exhibited short term strength increases due to blunting of crack tips, though at longer exposure times strength decreases due to oxidation pit formation (Ref. 116). High temperature oxidative environments can also adversely effect crack growth and enhance creep (Ref. 117). Sintering additives play a major role in oxidation rate and mechanical properties. An addition of 12.5 w/o Lu_2O_3 to Si_3N_4 significantly improves its high temperature ($\geq 1400^\circ\text{C}$) strength due to formation of a high temperature grain boundary phase which extensively crystallizes during processing (Ref. 118).

As discussed earlier, both active oxidation to $\text{SiO}(\text{g})$ and water vapor reactions to form $\text{Si}(\text{OH})_4(\text{g})$ lead to material consumption. After 20 h at 1400°C and a $P(\text{O}_2) = 1.5 \times 10^{-5}$ MPa, α -SiC exhibits a 50% reduction in strength due to pit formation from active oxidation (Ref. 43). In a high velocity combustion rig, the surface oxide is continually swept away by its reaction with water vapor. For Si_3N_4 after 100 h at 1400°C, exposure with 5 bar total pressure in a natural gas burner (and corresponding water vapor content) results in strength reductions of 20-70% (Ref. 113).

Corrosion of SiC by molten salts, either by thin films (Ref. 119) or continuous deposition (Ref. 120), results in surface pit formation and resultant strength loss. Pits occur where gas bubbles form at the substrate-liquid silicate interface, continually exposing the substrate to corrosion. Burner rig hot corrosion of a Y-containing Si_3N_4 results in modification of near-surface grain boundaries and subsequent strength loss (Ref. 121).

Due to the complex nature of CMCs, differing modes of attack occur as a function of temperature. As discussed, the major issue with continuous fiber reinforced CMCs is the easily oxidizable second phase (e.g. C or BN). If the second phase is exposed to oxygen and/or water vapor due to a crack or discontinuous outer protective oxide, degradation will occur. Stress rupture life of a crack-free, as-produced SiC/SiC composite with BN fiber interphase at 815°C in air under 140 MPa tensile load is 50h. Stress-rupture life of the pre-cracked material under the

same conditions was less than 5 h (Ref. 122). For a carbon-fiber reinforced SiC matrix, attack of the fiber has an adverse effect on stress rupture behavior (Ref. 123). The effect of environment on mechanical properties of CMCs is a critical area of research.

High Temperature Wear of Advanced Ceramics

The brittle nature of most monolithic ceramics has largely precluded their use in applications where high tensile stresses occur. One such example is in dry sliding contact, where high friction forces can result in significant tensile stresses, even under modest loads, leading to fracture and subsequent wear (Ref. 124). The development in recent decades of advanced ceramics with engineered microstructures has resulted in markedly improved strength and toughness properties (Ref. 125). Certain ceramics, such as silicon nitride, achieve excellent toughness by tailoring the grain size and composition of grain boundary phases (Ref. 126). Others, such as alumina, are strengthened by the addition of secondary phases based upon zirconia and silicon carbide whiskers intended to enhance favorable residual compressive stresses and deflect and halt crack propagation (Ref. 127). The engineering promise of advanced ceramics has been further enhanced by improved finishing technologies capable of generating precise and complex part geometries with significantly reduced flaw sizes. The emergence of these new ceramics in the early 1980's enabled consideration of several demanding high temperature applications.

Two such applications involved heat engine components; ceramic gas turbines and adiabatic diesels (Refs. 128,129). An important characteristic for these and other applications are tribological, or friction and wear, properties particularly in sliding contact at high temperatures under dry, non-lubricated conditions. Unfortunately, extensive and reliable data regarding the high temperature tribological properties of advanced ceramics has not been available, due to a lack of suitable test capabilities and lack of characterization of these newer ceramics and composites.

Initially, many in the research community hypothesized that advanced ceramics might exhibit favorable high temperature friction and wear properties because of their high hot hardness and low achievable surface roughness characteristics. This concept was loosely based upon the premise that friction and wear, for self mated steel for instance, was due to local surface asperity interactions in which contact points of surfaces resulted in local hot spots, adhesive welding and

material oxidation. Therefore, it was considered that the hard, smooth and chemically non-reactive ceramics would not suffer from such wear mechanisms.

More recent tribological studies of many classes of nitride, carbide, oxide and composite ceramics, however, have revealed that, in general, ceramics exhibit high friction and wear in non-lubricated, high temperature sliding contacts (Refs. 130-135). Table VI summarizes measured friction and wear factor coefficients for a variety of ceramics from self mated ceramic pin-on-disk tests at temperatures from 25 to up to 1200°C. Typical tests are 1 hr for a total sliding distance of 9.7 km. Observed steady state friction coefficients range from about 0.5 to 1.0 or above. Often, during initial sliding especially at room temperatures, lower values are observed. Typically these are attributed to surface contamination and adsorbed layers being quickly removed by the sliding process leading to the higher steady-state friction values. Wear factor coefficients, defined as the wear volume(mm^3) per distance slid(m) per load(N) are also very high but, as is typical for wear data, are more scattered and range from about 10^{-5} to 10^{-2} $\text{mm}^3/\text{N}\cdot\text{m}$. By comparison, oil lubricated steel sliding results in friction coefficients of 0.1 or less and wear factors less than 10^{-9} $\text{mm}^3/\text{N}\cdot\text{m}$.

Microscopic analyses of worn ceramic surfaces reveal two major modes of wear: brittle fracture and tribo-oxidative wear. High friction coefficients during sliding generate high tensile stresses in the wake of the contact area (Ref. 124). If sufficiently large flaws exist, cracks form, grow and ultimately lead to faceted wear debris formation. Figure 20 shows such features. Brittle wear predominates at lower temperatures for all ceramics and at high temperatures brittle behavior is a common feature for oxide materials like alumina. Nitride and carbide containing ceramics, however, when sliding at high temperature in air form complex and often glassy oxide surface layers which are removed by the sliding counter-face revealing fresh, non-oxidized surfaces. These then oxidize, resulting in an oxidative type wear process. The wear debris from these tests is often characterized by smeared oxide layers and sometimes even "rolled up" layered debris. Figure 21 shows an example of such oxide layer wear debris. In both cases, brittle fracture or oxide layer removal, wear rates are high.

Notwithstanding their poor self-lubricating properties, ceramics possess useful thermal, physical and chemical properties enabling their use in high temperature applications, provided their shortcomings are accommodated. For instance, using silicon nitride at lower temperatures in the presence of oil has enabled long life diesel engine components such as fuel

injectors and valve train components. The generally high stiffness and low density of ceramic materials also reduce dynamic forces in high speed components such as bearing balls. Hybrid ceramic bearings utilizing silicon nitride rolling elements and steel races are capable of significantly higher speeds than comparable all steel bearings under oil-lubricated conditions. Further, if contact loads can be sufficiently reduced, friction coefficients of 0.5 or higher can be tolerated in order to take advantage of ceramics excellent chemical inertness and dimensional stability. Finally, efforts are underway to add self-lubricating materials to ceramics such as graphite and boron nitride to mitigate high friction and wear without adversely affecting strength and other properties. As these research efforts progress, advanced ceramics will find ever increasing applications in engineering and technology.

Pin Material	Disk Material	Test Temperature, °C	Friction Coefficient	Average Wear Coefficient, mm ³ /N-m	Observed Wear Mode	Reference
Al ₂ O ₃	Al ₂ O ₃	25	0.84	10 ⁻⁷	microfracture	131
Al ₂ O ₃	Al ₂ O ₃	1000	0.50	10 ⁻⁷	microfracture	131
SiC	SiC	25	0.75	10 ⁻⁷		
SiC	SiC	1000	0.77	10 ⁻⁵	Oxide-layer removal	131
Si ₃ N ₄	Si ₃ N ₄	25	0.60	10 ⁻⁵	microfracture	130
Si ₃ N ₄	Si ₃ N ₄	1000	0.70	10 ⁻²	Oxide-layer removal	130
*Al ₂ O ₃ -SiC _w	Al ₂ O ₃ -SiC _w	25	0.74	10 ⁻⁷	microfracture	134
Al ₂ O ₃ -SiC _w	Al ₂ O ₃ -SiC _w	1200	0.58	10 ⁻⁶	microfracture-oxidation	134
ZrO ₂	ZrO ₂	25	0.68	10 ⁻⁴	microfracture	135
ZrO ₂	ZrO ₂	800	0.65	10 ⁻⁴	microfracture	135

*Al₂O₃-SiC_w is alumina with 25 volume percent silicon carbide whiskers added

Table VI- Friction and Wear Summary for Pin-on-Disk Sliding of Ceramics

Further Reading

1. N. S. Jacobson, *J. Am. Ceram. Soc.*, Vol. 76, (No. 1), 1993, p 3-28.
2. E. J. Opila and N. S. Jacobson, Corrosion of Ceramic Materials, *Materials Science and Technology: A Comprehensive Treatment, Corrosion and Environmental Degradation, Vol. II*, M. Schütze, Ed., Wiley-VCH, 2000, p 327-388.
3. N. S. Jacobson, D. S. Fox, J. L. Smialek, E. J. Opila, P. F. Tortorelli, K. L. Moore, K. G. Nickel, T. Hirata, M. Yoshida, and I. Yuri, Corrosion Issues for Ceramics in Gas Turbines, *Ceramic Gas Turbine Component Development And Characterization*, M. van Roode, M. K. Ferber, and D. W. Richerson, ASME Press, 2003, p 607-640.
4. T. Narushima, T. Goto, T. Hirai, and Y. Iguchi, *Mat. Trans. JIM*, Vol. 38, (No. 10) 1997, p 821-835.
5. K. G. Nickel and Y. G. Gogotsi, Corrosion of Hard Materials, *Handbook of Ceramic Hard Materials, Vol. 1*, R. Riedel, Ed., Wiley-VCH, 2000, p 140-182.

References

1. C. E. Ramberg, G. Cruciani, K. E. Spear, R. E. Tressler, and C. E. Ramberg, Jr., *J. Am. Ceram. Soc.* Vol. 79, (No. 11), 1997, p 2897-911.
2. D. S. Fox, *J. Am. Ceram. Soc.* Vol. 81, (No. 4), 1998, p 945-50.
3. B. E. Deal and A. S. Grove, *J. Appl. Phys.* Vol. 36, (No. 12), 1965, p 3770-78.
4. F. J. Norton, *Nature*, Vol. 171, 1961, p 701.
5. F. S. Pettit, *Trans. Met. Soc. AIME*, Vol. 239, 1967, p 1296-1302.
6. W. C. Hagel, *Trans. ASM*, Vol. 56, 1963, p 583-99.
7. K. Motzfeld, *Acta. Chem. Scand.*, Vol. 18, 1964, p 1696-706.
8. L. U. J. T. Ogbuji and E. J. Opila, *J. Electrochem. Soc.*, Vol. 142, (No. 3), 1995, p 925-930.
9. R. C. A. Harris, *J. Am. Ceram. Soc.* Vol. 58, (Nos. 1/2), 1984, p 7-9.
10. J. A. Costello and R. E. Tressler, *J. Am. Ceram. Soc.*, Vol. 64, (No. 6), 1986, p 674-681.
11. Z. Zheng, R. E. Tressler, and K. E. Spear, *J. Electrochem. Soc.*, Vol. 137, (No. 3), 1990, p 854-858.
12. L. U. J. T. Obuji, *J. Am. Ceram. Soc.*, Vol. 80, (No. 6), 1997, p 1544-1550.
13. G. C. Rybicki and J. L. Smialek, *Oxid. Met.*, Vol. 31, (Nos. 3/4), 1989, p 275-304.
14. D. Das, J. Farjas, and P. Roura, *J. Am. Ceram. Soc.*, Vol. 87, (No. 7), 2004, p 1301-1305.
15. R. Okada and R. Iijima, *Appl. Phys. Lett.*, Vol. 58, (No. 15), 1991, p 1662-1663.

16. D. S. Fox, E. J. Opila, Q. N. Nguyen, D. L. Humphrey, and S. Lewton, *J. Am. Ceram. Soc.*, Vol. 86, (No. 8), 2003, p 1256-1281.
17. H. Du, R. E. Tressler, K. E. Spear, and C. G. Pantano, *J. Electrochem. Soc.*, Vol. 136, (No. 5), 1989, p 1527-1536.
18. K. L. Luthra, *J. Am. Ceram. Soc.* Vol. 74, (No. 5), 1991, p 1095-1103.
19. L. U. T. Ogbuji and D. T. Jayne, *J. Electrochem. Soc.* Vol. 140, (No. 3), 1993, p 759-766.
20. D. Cubicciotti and K. H. Lau, *J. Am. Ceram. Soc.*, Vol. 61, (No. 11-12), 1978, p 512-517.
21. D. Cubicciotti and K. H. Lau, *J. Electrochem. Soc.*, Vol. 126, (No. 10), 1979, p 1724-1728.
22. P. Andrews and F. L. Riley, *J. Eur. Ceram. Soc.* Vol. 7, 1991, p 125-132.
23. S. C. Singhal and F. F. Lange, *J. Am. Ceram. Soc.* Vol. 58, (Nos. 9-10), 1975, p 433-435.
24. N. S. Jacobson, *J. Am. Ceram. Soc.*, Vol. 76, (No. 1), 1993, p 3-28.
25. E. J. Opila, D. S. Fox, and C. A. Barrett, Cyclic oxidation of monolithic SiC and Si₃N₄ materials, *Ceram. Eng. Sci. Proceedings*, Vol. 14, (No. 7-8), 1993, p 367-374.
26. E. J. Opila and N. S. Jacobson, Corrosion of Ceramic Materials, *Materials Science and Technology: A Comprehensive Treatment, Corrosion and Environmental Degradation, Vol. II*, M. Schütze, Ed., Wiley-VCH, 2000, p 327-388.
27. E. J. Opila, *J. Am. Ceram. Soc.*, Vol. 77, (No. 3), 1994, p 730-736.
28. E. J. Opila and R. E. Hann, Jr., *J. Am. Ceram. Soc.*, Vol. 80, (No. 1), 1997, p 197-205.
29. N. S. Jacobson, E. J. Opila, D. Myers, and E. Copland, Thermodynamics of the Gas Phase Species in the Si-O-H System, to appear in *J. Chem. Therm.*
30. W. M. Kays and M. E. Crawford, *Convective Heat and Mass Transfer*, McGraw-Hill, 1980, p 139, 197.
31. R. C. Robinson and J. L. Smialek, *J. Am. Ceram. Soc.*, Vol. 82, (No. 7), 1999, p 1817-1825.
32. E. J. Opila, J. L. Smialek, R. C. Robinson, D. S. Fox, and N. S. Jacobson, *J. Am. Ceram. Soc.* Vol. 82, (No. 7), 1999, p 1826-1834.
33. I. Yuri and T. Hisamatsu, Recession Rate Prediction for Ceramic Materials in Combustion Gas Flow, *ASME TURBO EXPO 2003*, American Society of Mechanical Engineers, 2003.
34. R. C. Robinson and J. L. Smialek, Durability of Ceramic Matrix Composites in Combustion Environments, *Electrochemical Society Proceedings*, Vol. 99-38, M. McNallan, E. Opila, T. Maruyama, and T. Narita, Eds., Electrochemical Society, 2000, p 407-417.
35. J. L. Smialek, R. C. Robinson, E. J. Opila, D. S. Fox, and N. S. Jacobson, *Adv. Comp. Mat.*, Vol. 8, (No. 1), 1999, p 33-45.
36. C. Wagner, *J. Appl. Phys.*, Vol. 29, (No. 9), 1958, p 1295-1297.
37. S. C. Singhal, *Ceramurgia Int.*, Vol. 2, (No. 3), 1976, p 123-130.

38. T. Narushima, T. Goto, T. Hirai, and Y. Iguchi, *Mat. Trans. JIM*, Vol. 38, (No. 10) 1997, p 821-835.
39. D. E. Rosner and H. D. Allendorf, *J. Chem. Phys.*, Vol. 74, (No. 9), 1970, p 1829-1839.
40. W. L. Vaughn and H. G. Maahs, *J. Am. Ceram. Soc.*, Vol. 73, (No. 6), 1990, p 1540-1543.
41. J. W. Hinze and H. C. Graham, *J. Electrochem. Soc.* Vol. 123, (No. 7), 1976, p 1066-1073.
42. E. A. Gulbransen, K. F. Andrew, and F. A. Brassart, *J. Electrochem. Soc.*, Vol. 113, (No. 12), 1966, p 1311-1314.
43. M. Balat, G. Flamant, G. Male, and G. Pichelin, *J. Mat. Sci.*, Vol. 27, 1992, p 697-703.
44. T. Narushima, T. Goto, Y. Iguchi, and T. Hirai, *J. Am. Ceram. Soc.* Vol. 74, (No. 10) 1991, p 2583-2586.
45. H. -E. Kim and A. J. Moorhead, *J. Am. Ceram. Soc.*, Vol. 73, (No. 7), 1990, p 1868-1872.
46. N. S. Jacobson, K. N. Lee, and D. S. Fox, *J. Am. Ceram. Soc.*, Vol. 75, (No. 6), 1992, p 1603-1611.
47. E. J. Opila, *J. Am. Ceram. Soc.*, Vol. 78, (No. 4), 1995, p 1107-1110.
48. V. Pareek and D. A. Shores, *J. Am. Ceram. Soc.*, Vol. 74, (No. 3), 1991, p 556-563.
49. Z. Zheng, R. E. Tressler, K. E. Spear, *Corros. Sci.*, Vol 33, (No. 4), 1992, p 545-556.
50. Z. Zheng, R. E. Tressler, K. E. Spear, *Corros. Sci.*, Vol. 33, (No. 4), 1992, p 569-580.
51. Y. Cheong, P. Mukundhan, H. Du, and S. P. Withrow, *J. Am. Ceram. Soc.*, Vol. 83, (No. 1), 2000, p 154-160.
52. Y. Cheong, P. Mukundhan, H. Du, and S. P. Withrow, *J. Am. Ceram. Soc.*, Vol. 83, (No. 1), 2000, p 161-165.
53. P. Mukundhan, H. Du, and S. P. Withrow, *J. Am. Ceram. Soc.*, Vol. 85, (No. 4), 2002, p 865-872.
54. F. J. Kohl, C. A. Stearns, and G. C. Fryburg, Sodium Sulfate: Vaporization Thermodynamics and Role in Corrosive Flames, *Metal-Slag-Gas Reactions and Processes*, Z. A. Foroulis and W. W. Smeltzer, Eds., The Electrochemical Society, 1975, p 649-664.
55. R. A. Rapp, *Corros. Sci.*, Vol. 42, (No. 10), 1986, p 568-577.
56. F. S. Pettit and C. S. Giggins, Hot Corrosion, *Superalloys II*, C. T. Sims, N. S. Stoloff, and W. C. Hagel, Eds., Wiley, 1987, p 327-354.
57. S. Gordon and B. J. McBride, *Computer Program for Calculation of Complex Chemical Equilibrium Compositions, Rocket Performance, Incident and Reflected Shocks, and Chapman-Jouguet Detonations*, NASA SP-273, 1971.
58. N. S. Jacobson, *Oxid. Met.*, Vol. 31, (Nos. 1/2), 1989, p 91-103.
59. D. L. Deadmore, C. E. Lowell, and F. J. Kohl, *Corr. Sci.*, Vol. 19, 1979, p 371-378.

60. N. S. Jacobson and J. L. Smialek, *J. Am. Ceram. Soc.*, Vol. 68, (No. 8), 1985, p 432-439.
61. T. Sun, G. R. Pickrell, and J. J. Brown, Jr., *J. Am. Ceram.*, Vol. 77, (No. 12), 1994, p 3209-3214.
62. H. Flood and T. Förland, *Acta Chemica Scand.*, 1, 1947, p 592-604.
63. C. W. Bale, P. Chartrand, S. A. Degterov, G. Eriksson, K. Hack, R. Ben Mahfoud, J. Melancon, A. D. Pelton, and S. Petersen, *CALPHAD*, Vol. 26, (No. 2), 2002, p. 189-228.
64. M. I. Mayer and F. L. Riley, *J. Mater. Sci.*, Vol. 13, 1978, p 1319-1328.
65. M. K. Ferber, J. Ogle, V. J. Tennery, and T. Henson, *J. Am. Ceram. Soc.*, Vol. 68, (No. 4), 1985, p 191-197.
66. R. Raj, L. An, S. Shah, R. Riedel, C. Fasel, and H.-J. Kleebe, *J. Am. Ceram. Soc.*, Vol. 84, (No. 8), 2001, p 1803-1810.
67. H. P. Baldus, M. Jansen, *Angew Chem Int Ed Engl*, Vol. 36, 1997, p. 328-343.
68. A. Muller, P. Gerstel, E. Butchereit, K. G. Nickel, F. Aldinger, *J. Eur. Ceram. Soc.*, Vol. 24, (No. 12), 2004, p 3409-3417.
69. N. S. Jacobson, E. J. Opila, K. N. Lee, *Curr. Opinion in Sol. State & Mat. Sci.*, Vol. 5, 2001, p. 301-309.
70. A. G. Evans, *J. Am. Ceram. Soc.*, Vol. 73, (No. 2), 1990, p 187-206.
71. R. Naslain, *Adv. Comp. Mat.*, Vol. 8, 1999, p 3-16.
72. F. Lamouroux, G. Camus, J. Thebault, *J. Am. Ceram. Soc.*, Vol. 77, (No. 8), 1994, p 2049-3057.
73. M. C. Halbig and J. D. Cawley, Modeling the Environmental Effects on Carbon Fibers in a Ceramic Matrix at Oxidizing Conditions, *Proceedings of the 24th Annual Cocoa Beach Conference, American Ceramic Society*, Westerville, OH, 2000, p 219-226.
74. R. T. Bhatt, Oxidation Effects on the Mechanical Properties of SiC Fiber-Reinforced Reaction-Bonded Silicon Nitride Matrix Composites, NASA TM 102360, 1989.
75. L. Filipuzzi, G. Camus, R. Naslain, J. Thebault, *J. Am. Ceram. Soc.*, Vol. 77, (No. 2), 1994, p 459-466.
76. L. Filipuzzi and R. Naslain, *J. Am. Ceram. Soc.* 77, (No. 2), 1994, p 467-480.
77. N. S. Jacobson, G. N. Morscher, D. R. Bryant, and R. E. Tressler, *J. Am. Ceram. Soc.*, Vol. 82, (No. 6), 1999, p 1473-1482.
78. E. Opila, N. Jacobson, D. Humphrey, T. Yoshio, and K. Oda, The Oxidation of AlN in Dry and Wet Oxygen, *Electrochemical Society Proceedings*, Vol. 98-9, P. Y. Hou, M. J. McNallan, R. Oltra, E. J. Opila, and D. A. Shores, Eds., The Electrochemical Society, Pennington, NJ, 1998, p 430-437.

79. N. S. Jacobson, S. Farmer, A. Moore, and H. Sayir, *J. Am. Ceram. Soc.* Vol. 82, (No. 2), 1999, p 393-398.
80. N. J. Shaw, J. A. DiCarlo, N. S. Jacobson, S. R. Levine, J. A. Nesbitt, H. B. Probst, W. A. Sanders, and C. A. Stearns, *Materials for Engine Applications Above 3000°F—an Overview*, NASA TM 100169, 1987.
81. K. L. Luthra and H. D. Park, *J. Am. Ceram. Soc.*, Vol. 73, (No. 4), 1990, p. 1014-1023.
82. E. J. Opila, and N. S. Jacobson, Volatile Hydroxide Species of Common Protective Oxides and their Role in High Temperature Corrosion, *Electrochemical Society Proceedings*, Vol. 96-26, R. A. Rapp, D. A. Shores, and P. Y. Hou, Eds., Electrochemical Society, 1997, p 269-280.
83. A. Hashimoto, *Geochimica et Cosmochimica Acta*, Vol. 56, 1992, p 511-532.
84. O. H. Krikorian, *High Temp-High Press.*, Vol 14, 1982, p 387-397.
85. F. S. Pettit, G. H. Meier, and J. R. Blachere, Oxide Ceramics, *Environmental Effects on Engineered Materials*, R. H. Jones, Ed., Marcel Dekker, 2001, p 351-374.
86. R. L. Jones, Vanadate-sulfate Melt Thermochemistry Relating to Hot Corrosion of Thermal Barrier Coatings, Naval Research Laboratory, NRL/MR/6170—97-8103, 1997.
87. K. N. Lee, H. Fritze, and Y. Ogura, Coatings for Engineering Ceramics, *Progress in Ceramic Gas Turbine Development*, Vol. 2. M. van Roode, M. Ferber, and D. W. Richerson, Eds., ASME Press, 2003, p 641-664.
88. K. N. Lee, *Surface and Coatings Technology*, Vol. 133-134, 2000, p 1-7.
89. K. N. Lee, D. S. Fox, and N. P. Bansal, *J. Euro. Ceramic. Soc.* in press.
90. K. N. Lee, R. A. Miller, and N. S. Jacobson, *J. Am. Ceram. Soc.*, Vol. 78, (No. 3), 1995, p 705-710.
91. S. N. Basu, P. Hou, and V. K. Sarin, *International Journal of Refractory Metals & Hard Materials*, Vol. 16, 1998, p 343-352.
92. J. A. Haynes, M. J. Lance, K. M. Cooley, M. K. Ferber, R. A. Lowden, and D. P. Stinton, *J. Am. Ceram. Soc.*, 83 [3], 657-659 (2000).
93. J. I. Federer, *J. Mater. Eng.*, Vol. 12, 1990, p 141-149.
94. N. S. Jacobson, K. N. Lee, and Y. Yoshio, *J. Am. Ceram. Soc.*, Vol. 79, (No. 8), 1996, p 2161-2167.
95. W. Y. Lee, K. L. More and Y. W. Bae, *J. Am. Ceram. Soc.* Vol. 79, (No. 9), 1996, p 2489-2492.
96. K. N. Lee, D. S. Fox, J. I. Eldridge, D. Zhu, R. C. Robinson, N. P. Bansal, and R. A. Miller, *J. Am. Ceram. Soc.*, Vol. 86, (No. 8), 2003, p 1299-1306.
97. K. N. Lee, J. I. Eldridge, and R. C. Robinson, submitted to *J. Am. Ceram. Soc.*

98. K. N. Lee, *Transactions of the ASME*, Vol. 122, 2000, p 632-636.
99. H. E. Eaton, G. D. Linsey, E. Y. Sun, K. L. More, J. B. Kimmel, J. R. Price, and N. Miriyala, EBC Protection of SiC/SiC Composites in the Gas Turbine Combustion Environment -- Continuing Evaluation and Refurbishment Considerations, *ASME Turbo Expo 2001*, 2001-GT-0513, American Society of Mechanical Engineers, 2001.
100. K. L. More, P. F. Tortorelli, L. R. Walker, J. B. Kimmel, N. Miriyala, J. R. Price, H. E. Eaton, E. Y. Sun, and G. D. Lindsey, Evaluating Environmental Barrier Coatings on Ceramic Matrix Composites after Engine and Laboratory Exposures, *ASME Turbo Expo 2002*, 2002-GT-30630, American Society of Mechanical Engineers, 2002.
101. K. N. Lee, Multilayer Article Characterized by Low Coefficient of Thermal Expansion Outer Layer, 2004, US patent 6,759,151.
102. C. M. Weyant, K. T. Faber, J. D. Almer, and J. V. Guibeen, submitted to *J. Am. Ceram. Soc.*
103. W. Y. Lee, Y. W. Bae, and D. P. Stinton, *J. Am. Ceram. Soc.*, Vol. 78, (No. 7), 1995, p 1927-1930.
104. S. Ueno, N. Kondo, D. D. Jayaseelan, T. Ohji, and S. Kanzaki, High Temperature Hydro Corrosion Resistance of Silica Based Oxide Ceramics, *Proceedings of IGTI2003 ASME Turbo Expo 2003*, 2003-GT-38878, ASME.
105. S. Ueno, D. D. Jayaseelan, and T. Ohji, *Int. J. Appl. Technol.*, Vol. 1, (No. 4), 2004, p 362-373.
106. H. Klemm, M. Fritsch, and B. Schenk, Corrosion of Ceramic Materials in Hot Gas Environment, *Ceramic Engineering and Science Proceedings*, Vol. 25, (Nos. 3-4), E. Lara-Curzio and M. J. Readey, Eds., 2004, p. 463-468.
107. Y. Harada, T. Suzuki, K. Hirano, N. Nakagawa, and Y. Waku, Effect of Water Vapor in Degradation of in-situ Single-Crystal Oxide Eutectic Composites, *Fifth International Conference on High Temperature Ceramic Matrix Composites*, M Singh, R. J. Kerans, E. Lara-Curzio, and R. Naslain, eds., American Ceramic Society, 2004, p 389-394.
108. H. Nakayama, K. Aoyama, M. Yamamoto, H. Sumitomo, K. Okamura, T. Yamamura, and M. Sato, Evaluation of Environmental Barrier Coatings for CRCC in the High-Water-Vapor-Pressurized Environments at High Temperatures, *Fifth International Conference on High Temperature Ceramic Matrix Composites*, M Singh, R. J. Kerans, E. Lara-Curzio, and R. Naslain, eds., American Ceramic Society, 2004, p 613-618.

109. T. Ohji, Environmental Barrier Coating on Silicon Nitride; Challenges and Critical Issues, presented at the 28th International Conference and Exposition on Advanced Ceramics and Composites, Cocoa Beach, FL, 2004.
110. I. Yuri, T. Hisamatsu, S. Ueno, and T. Ohji, ASME Turbo Expo 2004, GT2004-54277, American Society of Mechanical Engineers, 2004.
111. S. Ueno, D. D. Jayaseelan, N. Kondo, T. Ohji, and S. Kanzaki, *J. Mat. Sci.*, Vol. 39, 2004, p 6627-6629.
112. S. R. Choi, J. M. Pereira, L. A. Janosik and R. T. Bhatt, *Mat. Sci & Engr. A*, Vol. 379, 2004, p 411-419.
113. H. Klemm, *J. Eur. Ceram. Soc.*, Vol. 22, 2002, p 2735-2740.
114. Saint-Gobain Ceramics, Datasheet B-1045, Niagara Falls, NY, 2003, p 3.
115. P. F. Becher, *J. Am. Ceram. Soc.*, Vol. 66, (No. 8), 1983, p C120-C121.
116. T. E. Easler, R. C. Bradt, and R. E. Tressler, *J. Am. Ceram. Soc.*, Vol. 65 (No. 6), 1982, p 317-320.
117. R. E. Tressler, Environmental Effects on Long Term Reliability of SiC and Si₃N₄ Ceramics, *Corrosion and Corrosive Degradation of Ceramics*, R. E. Tressler and M. McNallen, Eds., The American Ceramic Society, Westerville, OH, 1989, p 99-124.
118. S. Guo, N. Hirosaki, Y. Yamamoto, T. Nishimura and M. Mitomo, *J. Am. Ceram. Soc.*, Vol. 86, (No. 11), 2003, p 1900-1905.
119. J. L. Smialek and N. S. Jacobson, *J. Am. Ceram. Soc.*, Vol. 69 (No. 10), 1986, p 741-752.
120. D. S. Fox and J. L. Smialek, *J. Am. Ceram. Soc.*, Vol. 73 (No. 2), 1990, p 303-311.
121. D. S. Fox, M. D. Cuy and T. E. Strangman, *J. Am. Ceram. Soc.*, Vol. 80 (No. 11), 1997, p 2798-2804.
122. G. N. Morscher and J. D. Cawley, *J. Eur. Ceram. Soc.*, Vol. 22, (No. 14-15), 2002, p 2777-2788.
123. M. J. Verrilli, E. J. Opila, A. Calomino and J. D. Kiser, *J. Am. Ceram. Soc.*, Vol. 87 (No. 8), 2004, p 1536-1542.
124. D. W. Richerson, L. J. Lindberg, W. D. Carruthers, and J. Dahn, Contact Stress Effects in Si₃N₄ and SiC Interfaces, *Ceramic Engineering Science Proceedings*, Vol. 2, 1981, p. 578-588.
125. C. H. E. Helms and S. R. Thrasher, *Engineering Applications of Ceramic Materials*, American Society for Metals, Metals Park, OH, 1985.
126. M. N. Gardos and R. G. Hardisty, *Tribology Transactions*, Vol. 36, (No.4), 1993, p 653-660.
127. P. F. Becher and T. N. Tiegs, *Advanced Ceramic Materials*, Vol. 3, 1988, p 148.

128. R. Kamo and W. Bryzik, *Lubrication Engineering*, Vol. 48, (No. 10), 1992, p 809-815.
129. Garret Turbine Engine Company, Advanced Gas Turbine (AGT) Powertrain System Development for Automotive Applications, Semiannual Progress Report Number 1, NASA Report CR-165175, 1980.
130. A. Skopp, M. Woydt and K. H. Habig, *Tribology International*, Vol. 23, (No. 3), 1990, p 189-199.
131. H. Wang, Y. Kimurs and K. Okada, Sliding Friction and Wear of Ceramics at Elevated Temperatures up to 1000°C, *Proceedings of the Japan International Tribology Conference*, 1990, p 1389-1394.
132. J. R. Gomes, M. I. Osendi, P. Miranzo, F. J. Oliveira and R. F. Silva, *Wear*, Vol. 233-235, 1999, p 222-228.
133. C. Melandri, M. G. Gee, G. de Portu and S. Guicciardi, *Tribology International*, Vol. 28, (No. 6), 1995, p 403-413.
134. C. Dellacorte, Tribological Character of SiC-whisker Reinforced Al₂O₃ at Elevated Temperatures, *Friction and Wear of Ceramics*, C. S. Jahanmir, Ed., Marcel-Dekker, Inc., NY, 1994, p 225-259.
135. H. E. Sliney and C. DellaCorte, *Lubrication Engineering*, Vol. 50, (No.7), 1993, p 571-576.
136. C. DellaCorte, S. C. Farmer, and P. O. Book, Experimentally Determined Wear Behavior of an Al₂O₃-SiC Composite from 25 to 1200°C, NASA TM 102549, 1990.

Figure Captions

1. Schematic of oxidation of a monolithic ceramic illustrating scale growth and substrate recession.
2. Oxidation kinetics for CVD SiC and CVD Si₃N₄ at 1300°C in oxygen. These data were taken with a TGA and converted to oxide thicknesses. (Source: Opila and Ogbuji, Ref. 8).
3. Arrhenius plot showing comparison of silica growth rate on silicon to those of growth rate of Cr₂O₃ on Cr and Al₂O₃ on Ni-Al.
4. Coefficient of thermal expansion for cristobalite and amorphous SiO₂, SiC, and Si₃N₄. (Adapted from: Jacobson, Ref. 24).
5. Cyclic oxidation weight change kinetics for SiC and Si₃N₄ in air at 1300°C with 5 h cycles. NT 154 Si₃N₄ contains about 4 w/o Y₂O₃. (Adapted from Opila, Fox, and Barrett, Ref. 25)
6. Volatilization of SiO₂ and parabolic behavior of CVD SiC and CVD Si₃N₄ in 50% H₂O/50% O₂ at 1200°C and a flow rate of 4.4 cm/sec. (Source: Opila and Jacobson, Ref. 26).
7. Weight loss of CVD SiC in a fuel-lean high pressure burner rig with gas velocities of 20 m/sec. (Adapted from Robinson and Smialek, Ref. 31).
8. SiC recession rates in a pressurized burner under fuel-lean conditions, 1200-1450°C, 4-15 atm, 10-27 m/s (Adapted from Robinson and Smialek, Ref. 31).
9. Measured and calculated active/passive transitions. The upper boundary Pⁱ(O₂)-W was calculated from Wagner's approach (equations 21,23; Ref. 36) and the lower boundary Pⁱ(O₂)-I was calculated from equation 22. Results are for the various types of SiC shown—chemically-vapor-deposited (CVD), single crystal (SC), and hot-pressed (HP). (Adapted from: Narushima et al., Ref. 38).
10. Calculated dew points for sodium sulfate deposition as a function of Na and S content in the fuel. (Source: Jacobson, Ref. 24).
11. Calculated phase diagram for Na₂O-SiO₂ showing phases as a function of Na₂O activity and absolute temperature. The critical boundary for stability of SiO₂ is in the lower portion of the diagram.
12. Polished cross section showing microstructure for sintered SiC (B, C additives) + one-time deposition of Na₂CO₃ as a source of Na₂O after 48 h at 1000°C in 0.1% CO₂/O₂ (Source: Jacobson, Ref. 24).
13. Optical micrographs of sintered SiC (B, C additives) after exposure in a Jet fuel burner rig at 1273 K (a) 46 h with no sodium (b) 13.5 hr with a sodium chloride seeded flame. (Source: Jacobson, Ref. 24).

14. TGA oxidation curves for a SiC fiber/Si₃N₄ matrix composite in flowing oxygen. Note the weight losses at the lower temperatures and protective behavior at the higher temperatures. (Source: Bhatt , Ref. 74).
15. Micrographs illustrating two types of behavior observed for oxidation of a SiC fiber/BN coating/SiC matrix composite. (a) Borosilicate glass formation after 100 h in oxygen at 816°C and (b) Volatilization of BN due to reaction with water after oxidation at 500°C in humid air (Source: Jacobson et al., Ref. 77).
16. Surface recession in 100 hours from isothermal oxidation for various ceramics, classified according to the protective oxide formed. (Adapted from: Shaw et al., Ref. 80)
17. Weight loss for coated and uncoated SiC in pressurized burner rig at 6 atm and 1230°C. Weight losses are due to formation of volatile hydroxides. (Source: Lee, Ref. 98)
18. Cross section of a Si/mullite + BSAS/BSAS coating on a SiC fiber/SiC matrix composite after furnace exposure, 90% H₂O/O₂, 1000 h, 1316°C, 1 h cycles. (Source: Lee, Ref. 89)
19. Cross section of a Si/mullite/Yb₂SiO₅ coating on a SiC fiber/SiC matrix composite after furnace exposure, 90% H₂O/O₂, 1000 h, 1380°C, 1 h cycles, showing good adherence, crack resistance and environmental stability.
20. TEM photomicrographs of cracks and faceted wear debris following room temperature sliding of an Al₂O₃-SiC_w whisker reinforced ceramic composite (Source: Dellacorte et al., Ref 136).
21. Ceramic wear debris formed from oxide layer removal on Al₂O₃-SiC_w disk specimen following 1200°C sliding in air (Source: Dellacorte et al., Ref. 136).